Soil Dynamics and Earthquake Engineering 166 (2023) 107736

Contents lists available at ScienceDirect

Soil Dynamics and Earthquake Engineering

journal homepage: www.elsevier.com/locate/soildyn

Wave-focusing to subsurface targets using a switching time-reversal mirror

Seungbum Koo [a], Heedong Goh [a], Loukas F. Kallivokas [a,b,*]

[a] Department of Civil, Architectural and Environmental Engineering, The University of Texas at Austin, Austin, 78712, TX, USA
[b] Oden Institute for Computational Engineering and Sciences, The University of Texas at Austin, Austin, 78712, TX, USA

ARTICLE INFO

Keywords:
Time reversal
Elastic wave focusing
Subsurface targets
Switching time reversal mirror

ABSTRACT

The need for wave energy focusing to selected targets embedded within a host is commonly shared among various engineering fields, whether for stimulation and imaging in exploration geophysics, or for contaminant removal in geo-environmental engineering, or even for diagnostic/therapeutic purposes in medicine. In this paper, we are concerned with the feasibility of focusing wave energy to multiple subsurface targets embedded within a semi-infinite heterogeneous elastic host, by exploiting the time-reversibility of the lossless wave equation under adverse conditions for time reversal. Of particular interest for practical applications in geophysics is the need for a switching time-reversing mirror, where recorded Dirichlet data must be time-reversed as Neumann data due to equipment constraints. In the absence of theoretical guarantees, we turn to numerical experiments and report that wave-focusing can be indeed realized, despite various departures from the theoretically ideal time reversal case.

1. Introduction

Stimulation of targets embedded in an arbitrarily heterogeneous medium by focusing wave energy to them can be a potent, non-invasive, recourse for imparting desired changes to the mechanical behavior of the targets. Key applications of wave stimulation include collapse of underground cavities/tunnels/mines/sink holes, wave-based enhanced oil recovery (EOR), removal of contaminant particles from aquifers or from the pores/interstices of geological formations, and others. Beyond geophysical, medical therapeutic applications are also among notable applications of wave-focusing, with lithotripsy being the archetypal case.

The typical – and most-researched to date – wave-focusing setting involves a target embedded in a finite domain occupied by an acoustic fluid. The target is surrounded by receivers/emitters that can record a signal originating from the target, and then the emitters can be used to redirect/focus energy to the target, by exploiting the time-reversibility of the wave equation [1]. By contrast, here we are interested in elastic wave-focusing, as opposed to acoustic, on targets embedded within the subsurface, i.e., hosted in a semi-infinite domain occupied by an elastic heterogeneous solid, without the benefit of having the targets surrounded by receivers and emitters, whether in the targets' vicinity or in the far field.

The present study is motivated by EOR considerations: there is interest in facilitating the mobility of oil ganglia in reservoir subregions typically bypassed by primary modes of recovery, especially in low permeability zones. The central hypothesis is that focusing wave energy to a target zone may induce sufficiently large matrix accelerations to overcome the capillary forces holding the ganglia in the pore space, thus setting the stage for conventional oil extraction methods to sweep the thus mobilized ganglia. Laboratory studies [2], field applications [3,4], and numerical studies [5–10] support the hypothesis.

It should be noted that, even though motivated by EOR needs, the applicability of elastic wave time reversal is much wider, encompassing health monitoring [11,12], geophysical probing [13], communications [14], and military applications alike [15]. Even more broadly, the time reversal (TR) concept can be used for chorochronic event localization for, e.g., the identification of the onset of a crack or of a fault rupture, both in space and time [16–22].

To set the stage, consider a three-dimensional semi-infinite domain, bounded by a flat surface, and occupied by an arbitrarily heterogeneous solid -a suitable ersatz for the subsurface. The interest is in focusing wave energy at specific subterranean targets. The targets are typically inclusions of rather limited and finite extent compared to their surroundings. To focus elastic wave energy to the targets, sources capable of initiating stress waves are used, placed either on the surface or at various depths below the surface. Surface sources capable of delivering elastic waves to the targets include Vibroseis trucks, whereas at-depth sources include wellbore hydraulic pumps, or other electro-mechanically activated loads.

The waves generated by any single one of these sources are typically omni-directional. The waves, as they travel through the medium

* Corresponding author at: Department of Civil, Architectural and Environmental Engineering, The University of Texas at Austin, Austin, 78712, TX, USA.
E-mail addresses: seungbum.koo@utexas.edu (S. Koo), heedong.goh@utexas.edu (H. Goh), loukas@mail.utexas.edu (L.F. Kallivokas).

https://doi.org/10.1016/j.soildyn.2022.107736
Received 7 October 2021; Received in revised form 15 December 2022; Accepted 21 December 2022
Available online 31 December 2022
0267-7261/

hosting the target, will lose energy due to three principal forms of attenuation: due to radiation damping because of expanding geometric fronts; due to intrinsic attenuation or material damping because of internal friction; and due to apparent attenuation because of scattering at grain or other material interfaces. Since there is no practical way of reducing or controlling the aforementioned sources of energy loss, focusing wave energy on a target requires that multiple sources are used, and, in fact, that they operate synergistically to, ideally, maximize the energy delivery to the target. In short, when operating multiple sources, conditions of constructive interference must be created at the target. To design a scheme that would allow all the waveform crests to arrive at the target simultaneously is fairly challenging even in the case of a homogeneous host, let alone in the case of an arbitrarily heterogeneous host, which is the typical setting in our application.

We are interested in devising a methodology that would, somehow, allow for the systematic illumination of the target, irrespective of the host's complexity. One such possible path is offered by a partial-differential-constrained optimization methodology [6,8,23]: accordingly, one can define a functional describing the sought outcome at the target (e.g., maximization of fluid pressure, or of kinetic energy, or of a pressure gradient, etc.), and treat the source signals (and their locations in space) as design parameters, which, upon the optimizer's convergence, would lead to wave sources that would have the desired effect on the target. In other words, one seeks to optimize the sources, with a particular outcome in mind, subject to the underlying physics of the problem at hand: this is the very setting of an *inverse source* problem [6,8]. As an inverse problem, its resolution is plagued by the usual difficulties associated with all inverse problems, including solution multiplicity and ill-conditioning. But, more importantly, the solution of the inverse source problem requires that the properties of the host and of the target be known *a priori*. In fact, the quality of the focusing is only as good as the information about the material properties of the host and the targets. In well-characterized subsurface formations, the properties may be *a priori* known with reasonable certainty, but never accurately, whereas in most other situations, the properties must be estimated prior to seeking to optimize the wave sources for purposes of focusing energy to a target. Thus, the source optimizer route, though technically feasible, depends greatly on knowing the properties, which is, in general, hindered by physical realities.

Given the difficulties associated with an inverse-source approach, it is of practical interest to explore alternatives that do not rely on *a priori* knowledge of the material distribution. Such an alternate route to focusing, and indeed the path followed herein, is based on the exploitation of the time reversal concept. The discussion of the methodology presented herein seeks to identify the factors that contribute to the loss or worsening of focusing resolution owing to the many physical constraints that force the less-than-ideal implementation of the time reversal concept in the field. The approach draws, wherever possible, from theoretical results, but, for the most part, rests on computational evidence.

Specifically, we are interested in the feasibility of focusing energy to multiple subsurface elastic targets embedded within a heterogeneous elastic host occupying a halfspace based on a time reversal approach, suitably adapted to field realities. As is well known, time reversal resides on the time-invariance of the lossless wave equation, when the direction of the time line is reversed.[1] Accordingly, when waves, emitted by a source, are first recorded at a TR mirror (TRM), and then time-reversed, the retransmitted waves, under ideal conditions, would refocus to the original source location. Departures from the ideal TR setting would result in resolution degradation; the setting discussed herein introduces several such departures. The unboundedness of the host, the inability to properly account for a sink at the source location during the TR step, the infeasibility of introducing non-silent initial conditions during the TR step to match the final conditions of the recording step, the need for a switching TR mirror, the limited aperture and density of the TR mirror, all conspire to degrade the focusing.

We note that a central difficulty to focusing stems from the character of the TRM: in the most common geophysical application of time-reversal, namely in source localization, displacements (or velocities) are recorded at the TRM, and are time-reversed during the transmitting step: that is, the same physical quantity is recorded and transmitted. In the wave-focusing field application of interest herein, the TRM character *switches* between the recorded and the transmitting steps: while displacements are still recorded at the TRM, the transmitting step involves tractions, since displacement time-histories cannot be physically imposed on the ground surface. Mathematically, the TRM switches from recorded Dirichlet data to transmitting Neumann data: there is no theoretical guarantee that a switching TRM would result in focusing, as the standard, non-switching, TRM would do.

We stress that in the literature, TR is often used to, for example, localize a source in the subsurface, by *computationally* time-reversing the records collected at the TRM. What is decidedly different between the most common usage of TR in the literature is that here we are concerned with the *physical* time-reversal of the TRM records to focus wave energy to a subterranean location: it is the physical realities in the field that impose a *switching* TR mirror.

In the absence of *a priori* information about the properties of the targets and the host, i.e., in the absence of an *a priori* known velocity model, the described inverse-source approach cannot be used, leaving only the possibility of blind excitations (e.g., [4]) as the means for stimulating a target formation. Thus, the primary goal of the approach we sketch below is to explore whether something better can be done, which would promote wave energy focusing at the targets, and appeal to the time-reversal concept to explore the feasibility of focusing, despite the presence of the aforementioned difficulties. In the following, we describe the theoretical framework and a few numerical experiments that seem to support the hypothesis that focusing is possible, in spite of the theoretical departures from the ideal time-reversal setting.

2. Multi-target time-reversal-based wave-focusing in a semi-infinite domain

The TR process involves two distinct steps: the recording step, when sensors located at the TR mirror record the wavefields generated due to the actuation of a source, and the transmitting step, when the recorded signals are time-reversed at the mirror and emitted therefrom. Both steps are described by the Navier equations of motions, subject to initial and boundary conditions, which are different for each one of the two steps. We describe next the numerical approach for simulating the wave motion in either of the two steps, in order to delineate the difficulties imposed by the field constraints.

2.1. Elastic wave propagation in a 3D heterogeneous PML-truncated domain

The physical problem involves an unbounded domain: for computational purposes, it is necessary to limit the unboundedness of the physical domain. To this end, we introduce Perfectly-Matched-Layers (PMLs), effecting domain truncation and the reduction of the semi-infinite domain to finite size, as shown in Fig. 1.

Specifically: the interior computational domain, occupied by a, generally, arbitrarily heterogeneous elastic and isotropic material, is denoted by Ω_{ID}; Ω_{INC} denotes the subsurface targets, which are, in general, elastic inclusions of properties different than the host; Ω_{PML} denotes the PML buffer zone, which envelops Ω_{ID}, except for the top (ground) surface, denoted by $\Gamma_{\text{ID}}^{\text{load}}$; $\Gamma_{\text{PML}}^{\text{free}}$ is the trace of the PML buffer

[1] The lossless wave equation contains a second-order derivative in time; time-invariance does not hold when first-order derivatives are present, as may be the case when material damping is assumed.

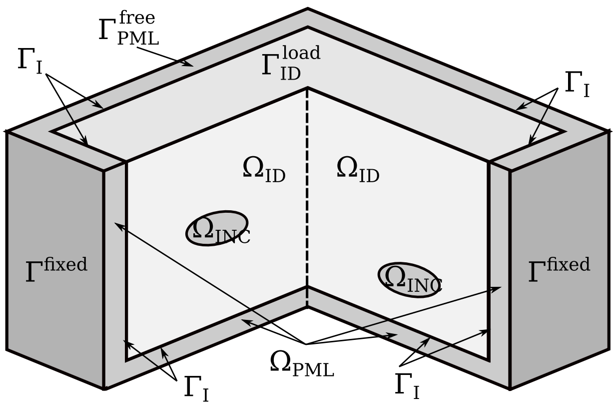

Fig. 1. Computational model of a semi-infinite, heterogeneous, isotropic, elastic domain containing target inclusions, terminated by Perfectly-Matched-Layers.

on the top surface; Γ_{I} denotes the interface between the interior domain Ω_{ID} and Ω_{PML}, and Γ^{fixed} denotes the outer boundary of the PML buffer.

We use a mixed-field PML formulation [24], where the motion within the interior domain Ω_{ID} is described solely by the displacement field $\mathbf{u}^{\mathrm{ID}}$, whereas the motion within the PML (Ω_{PML}) is described by both the displacement field $\mathbf{u}^{\mathrm{PML}}$ and the stress history field $\mathbf{S}$ (thence the mixed-field designation). The resulting equations of motion, where all functional dependence on space and time has been suppressed for brevity, can be succinctly cast as,

$$\mathcal{L}\left[\mathbf{u}^{\mathrm{ID}}\right] = -\,\mathbf{f}, \qquad \boldsymbol{x} \in \Omega_{\mathrm{ID}},\ t \in (0,T] \quad \text{and} \tag{1a}$$

$$\mathcal{M}\left[\mathbf{u}^{\mathrm{PML}}, \mathbf{S}\right] = \mathbf{0}, \qquad \boldsymbol{x} \in \Omega_{\mathrm{PML}},\ t \in (0,T]. \tag{1b}$$

In (1), the Navier operator $\mathcal{L}[\ ]$ is defined as:

$$\mathcal{L}[\ ] = \operatorname{div}\left\{\mu(\boldsymbol{x})\operatorname{grad}[\ ] + \mu(\boldsymbol{x})(\operatorname{grad}[\ ])^{\intercal} + \lambda(\boldsymbol{x})\operatorname{div}[\ ]\,\mathbf{I}\right\} - \rho(\boldsymbol{x})[\ddot{\ }], \tag{2}$$

where $\rho(\boldsymbol{x})$ denotes mass density, $\lambda(\boldsymbol{x})$ and $\mu(\boldsymbol{x})$ are the Lamé parameters, and a double overdot ($\ddot{\ }$) denotes second-order time derivative of the subtended quantity. The operator $\mathcal{M}$ for the PML is defined as:

$$\mathcal{M}\left[\mathbf{u}^{\mathrm{PML}}, \mathbf{S}\right] = \begin{bmatrix} \mathcal{P} & \mathcal{R} \\ \mathcal{S} & \mathcal{Q} \end{bmatrix} \begin{pmatrix} \mathbf{u}^{\mathrm{PML}} \\ \mathbf{S} \end{pmatrix}, \tag{3}$$

where

$$\mathcal{P}[\ ] = -\,\rho\left(\mathsf{a}[\dddot{\ }] + \mathsf{b}[\ddot{\ }] + \mathsf{c}[\dot{\ }] + \mathsf{d}[\ ]\right), \tag{4a}$$

$$\mathcal{R}[\ ] = \operatorname{div}\left([\ddot{\ }]^{\intercal}\Lambda_e + [\dot{\ }]^{\intercal}\Lambda_p + [\ ]^{\intercal}\Lambda_w\right), \tag{4b}$$

$$\begin{aligned}\mathcal{S}[\ ] = -\,\mu\,\big\{&\operatorname{grad}[\ddot{\ }]\Lambda_e + \Lambda_e(\operatorname{grad}[\ddot{\ }])^{\intercal} + \operatorname{grad}[\dot{\ }]\Lambda_p \\ &+ \Lambda_p(\operatorname{grad}[\dot{\ }])^{\intercal} + \operatorname{grad}[\ ]\,\Lambda_w \\ &+ \Lambda_w(\operatorname{grad}[\ ])^{\intercal}\big\} - \lambda\left\{\operatorname{div}\left(\Lambda_e[\ddot{\ }]\right) + \operatorname{div}\left(\Lambda_p[\dot{\ }]\right) + \operatorname{div}\left(\Lambda_w[\ ]\right)\right\}\mathbf{I}, \\ &\text{and}\end{aligned} \tag{4c}$$

$$\mathcal{Q}[\ ] = \mathsf{a}[\ddot{\ }] + \mathsf{b}[\ddot{\ }] + \mathsf{c}[\dot{\ }] + \mathsf{d}[\ ]. \tag{4d}$$

The definitions for the stretch tensors Λ_e, Λ_p, and Λ_w and the related PML parameters a, b, c, and d can be found in [24]. The boundary conditions for the PML, and the interface conditions are the same for both the recording and the transmitting steps, i.e., $\forall t \in (0,T]$,

$$\mathbf{u}^{\mathrm{PML}} = \mathbf{0}, \quad \boldsymbol{x} \in \Gamma^{\mathrm{fixed}}, \tag{5a}$$

$$\left[\ddot{\mathbf{S}}^{\intercal}\Lambda_e + \dot{\mathbf{S}}^{\intercal}\Lambda_p + \mathbf{S}^{\intercal}\Lambda_w\right]\mathbf{n}^{\mathrm{PML}} = \mathbf{0}, \quad \boldsymbol{x} \in \Gamma_{\mathrm{PML}}^{\mathrm{free}}, \tag{5b}$$

$$\mathbf{u}^{\mathrm{ID}} - \mathbf{u}^{\mathrm{PML}} = \mathbf{0}, \quad \boldsymbol{x} \in \Gamma_{\mathrm{I}}, \quad \text{and} \tag{5c}$$

$$\begin{aligned}&\left[\mu\operatorname{grad}\mathbf{u}^{\mathrm{ID}} + \mu\left(\operatorname{grad}\mathbf{u}^{\mathrm{ID}}\right)^{\intercal} + \lambda\left(\operatorname{div}\mathbf{u}^{\mathrm{ID}}\right)\mathbf{I}\right]\mathbf{n}^{\mathrm{ID}} \\ &\quad - \left[\ddot{\mathbf{S}}^{\intercal}\Lambda_e + \dot{\mathbf{S}}^{\intercal}\Lambda_p + \mathbf{S}^{\intercal}\Lambda_w\right]\mathbf{n}^{\mathrm{PML}} = \mathbf{0}, \quad \boldsymbol{x} \in \Gamma_{\mathrm{I}}.\end{aligned} \tag{5d}$$

In the above: (5a) is the fixed displacement condition on the outer PML boundary; (5b) denotes a traction-free condition on the $\Gamma_{\mathrm{PML}}^{\mathrm{free}}$; and (5c) and (5d) are the displacement and traction continuity conditions along the Γ_{I} interface. Moreover, $\mathbf{n}^{\mathrm{ID}}$ and $\mathbf{n}^{\mathrm{PML}}$ denote outward normal vectors on the boundaries of the interior and PML domains, respectively.

The initial and boundary value problem defined by (1), (3), and (5) is incomplete: its completion requires the specification of the missing conditions, which are different for the recording and the transmitting steps. The required conditions are addressed in the next two sections.

2.2. Time-reversal-based wave-focusing: the recording step

During the recording step, probes are placed inside the target inclusions Ω_{INC} (Fig. 1); when triggered, the sources are driven by signals $f(t)$. The set of all n probes is represented by the domain source $\mathbf{f}(\boldsymbol{x},t)$ in (1a), defined as:

$$\mathbf{f}(\boldsymbol{x},t) = \sum_n f(t)\,\delta\left(\boldsymbol{x} - \boldsymbol{x}_n\right), \qquad n \in \mathbb{Z},\ \boldsymbol{x}_n \in \Omega_{\mathrm{INC}}. \tag{6}$$

Then, the resulting displacement wavefields are recorded at the TRM sensors, which are mounted on the ground surface. We assume that the TRM has a negligible influence on the surface motion, and we, thus, consider $\Gamma_{\mathrm{ID}}^{\mathrm{load}}$ to be traction-free, i.e.:

$$\mathbf{t} = \mathbf{0}, \quad \boldsymbol{x} \in \Gamma_{\mathrm{ID}}^{\mathrm{load}}, \tag{7}$$

where $\mathbf{t} = \left[\mu\operatorname{grad}\mathbf{u}^{\mathrm{ID}} + \mu\left(\operatorname{grad}\mathbf{u}^{\mathrm{ID}}\right)^{\intercal} + \lambda\left(\operatorname{div}\mathbf{u}^{\mathrm{ID}}\right)\mathbf{I}\right]\mathbf{n}^{\mathrm{ID}}$ denotes surface traction. In summary, the complete statement for the recording step reads: given a domain source $\mathbf{f}$, find the displacement field $\mathbf{u}^{\mathrm{ID}}$ on $\boldsymbol{x} \in \Gamma_{\mathrm{ID}}^{\mathrm{load}}$ such that:

$$\mathcal{L}\left[\mathbf{u}^{\mathrm{ID}}\right] = -\mathbf{f}, \qquad \boldsymbol{x} \in \Omega_{\mathrm{ID}},\ t \in (0,T] \quad \text{and} \tag{8a}$$

$$\mathcal{M}\left[\mathbf{u}^{\mathrm{PML}}, \mathbf{S}\right] = \mathbf{0}, \qquad \boldsymbol{x} \in \Omega_{\mathrm{PML}},\ t \in (0,T], \tag{8b}$$

subject to silent initial conditions, and boundary and interface conditions (5) and (7).

2.3. Time-reversal-based wave-focusing: the transmitting step

During the transmitting step, the recorded displacement wavefield is time-reversed and used to drive applied surface tractions (instead of displacements), since equipment limitations do not allow for the application of a displacement field on the ground surface. Thus, the corresponding traction boundary condition becomes:

$$\mathbf{t}_{\mathrm{tr}}(\boldsymbol{x},t) = \alpha\mathbf{u}^{\mathrm{ID}}(\boldsymbol{x}, T - t), \quad \boldsymbol{x} \in \Gamma_{\mathrm{ID}}^{\mathrm{load}}, \tag{9}$$

where α is a constant used to force consistency in the dimensions (displacements to tractions), and the subscript $[\ ]_{\mathrm{tr}}$ denotes that the subscripted quantity is a transmitted field. Accordingly, since the character of the applied field at the TRM switches between the recording and the transmitting steps, whereby recorded Dirichlet data are transmitted as Neumann data, we term the mirror *a switching TRM*. We note that time-reversing Dirichlet data as Neumann data has been attempted in the scalar wave case [25], where it was shown that focusing is still possible, while, recently in Goh et al. [26] a filter was proposed to improve the focusing resolution when a switching TRM is used.

The switching TRM is not the only threat to the resolution quality. In general, since at the end of the recording step it holds that $\mathbf{u}^{\mathrm{ID}}(\boldsymbol{x},T) \neq \mathbf{0}$, for $\boldsymbol{x} \in \Omega_{\mathrm{ID}} \cup \Omega_{\mathrm{INC}} \cup \Omega_{\mathrm{PML}}$, then the initial conditions during the transmitting step cannot be silent. However, applying non-silent initial conditions throughout the domain, or even on part of it, is infeasible, and, thus, silent initial conditions are instead applied, which, as was shown in [27], would result in resolution degradation. Furthermore: theoretically, in an ideal time reversal application, the domain source $\mathbf{f}(\boldsymbol{x},t)$ in (8a) must also be time-reversed during the transmitting step, thus giving rise to a *sink*. The sink provides a (time-reversed) evanescent wavefield in the sink's vicinity, which greatly improves the resolution locally. However, the typical apparatus used as a source (or a sink) is amplitude-limited and would thus have very little effect during the transmitted step when the emitted field would be amplified.

With the above limitations in mind, the mathematical setting of the TR transmitting step becomes: find the displacement wavefield $\mathbf{u}_{\mathrm{tr}}^{\mathrm{ID}}$ such that:

$$\mathcal{L}\left[\mathbf{u}_{\mathrm{tr}}^{\mathrm{ID}}\right]=\mathbf{0}, \qquad \boldsymbol{x}\in\Omega_{\mathrm{ID}},\ t\in(0,T] \quad \text{and} \tag{10a}$$

$$\mathcal{M}\left[\mathbf{u}_{\mathrm{tr}}^{\mathrm{PML}},\mathbf{S}_{\mathrm{tr}}\right]=\mathbf{0}, \qquad \boldsymbol{x}\in\Omega_{\mathrm{PML}},\ t\in(0,T], \tag{10b}$$

subject to silent initial conditions, and the boundary and interface conditions (5) and (9).

3. Motion metrics for energy delivery

To assess the impact the various departures from the ideal TR case have on the focusing to subsurface targets, we adopt the motion metrics proposed in Koo et al. [9] and Karve et al. [23] in order to quantify the strength and the efficiency of the energy delivered to the targeted inclusions. Accordingly, we define:

1. The instantaneous kinetic energy $\mathrm{KE}_{\mathrm{INC}}(t)$ at the targeted inclusions as:

$$\mathrm{KE}_{\mathrm{INC}}(t)=\frac{1}{2}\int_{\Omega_{\mathrm{INC}}}\dot{\mathbf{u}}_{\mathrm{tr}}^{\mathrm{ID}}(\boldsymbol{x},t)\cdot\rho(\boldsymbol{x})\dot{\mathbf{u}}_{\mathrm{tr}}^{\mathrm{ID}}(\boldsymbol{x},t)\,d\Omega. \tag{11}$$

2. The time-averaged kinetic energy $\mathrm{KE}_{\mathrm{INC}}^{\mathrm{TA}}$ in the targeted inclusions is defined as:

$$\mathrm{KE}_{\mathrm{INC}}^{\mathrm{TA}}=\frac{1}{T_2-T_1}\int_{T_1}^{T_2}\mathrm{KE}_{\mathrm{INC}}(t)\,dt, \tag{12}$$

where $t\in(T_1,T_2)$ is an observation time window of interest.

3. The energy input $\mathrm{E}_{\mathrm{input}}$ is defined as:

$$\mathrm{E}_{\mathrm{input}}=\int_0^T\int_{\Gamma_{\mathrm{ID}}^{\mathrm{load}}}\mathbf{t}_{\mathrm{tr}}(\boldsymbol{x},t)\cdot\dot{\mathbf{u}}_{\mathrm{tr}}^{\mathrm{ID}}(\boldsymbol{x},t)\,d\Gamma\,dt. \tag{13}$$

4. The spatial distribution of the total energy $\mathrm{KE}^{\mathrm{TA}}$during the transmitting step is defined as:

$$\mathrm{KE}^{\mathrm{TA}}(\boldsymbol{x})=\frac{1}{2T}\int_0^T\mathbf{u}_{\mathrm{tr}}^{\mathrm{ID}}(\boldsymbol{x},t)\cdot\rho(\boldsymbol{x})\mathbf{u}_{\mathrm{tr}}^{\mathrm{ID}}(\boldsymbol{x},t)\,dt. \tag{14}$$

For example, we use the ratio $\mathrm{KE}_{\mathrm{INC}}^{\mathrm{TA}}/\mathrm{E}_{\mathrm{input}}$ to measure the efficiency of the energy delivered to the targeted inclusions, and we use $\mathrm{KE}^{\mathrm{TA}}(\boldsymbol{x})$ to plot the time-accumulated response within the computational domain for each numerical experiment to provide a visual aid for assessing focusing.

4. Numerical experiments on focusing feasibility

We report numerical experiments involving two targets embedded in a three-dimensional heterogeneous elastic host. We use the same model, as depicted in Fig. 2(a), for all simulations. Specifically, the domain of interest is a rectangular parallelepiped extending 80 m × 80 m on the surface, and 40 m-deep; it is surrounded by a 6.25 m-thick PML buffer on all of its sides, except on the surface. The host medium consists of a 20 m-deep layer resting on a halfspace. There are two soft, geometrically identical, oblate spheroidal inclusions embedded within the host. One of the spheroids is centered at (−15 m, −15 m, −20 m), effectively intersecting the layer interface, and the other is centered at (15 m, 15 m, −30 m). The three semi-axes of both spheroids are 7.5 m, 7.5 m, and 3.75 m, respectively. The first Lamé parameter (λ) of the top layer, the halfspace, and of the inclusions is 300 MPa, 500 MPa, and 100 MPa, respectively. The second Lamé parameter (μ) – the shear modulus – is equal to the first, since the Poisson's ratio has been set to 0.25 for all layers and inclusions. The mass density is $\rho=2000$ kg/m^3. The relative softness of the inclusions with respect to the surrounding layers is intended to mimic the contrast between shallow reservoirs and their host background.

The model is meshed with 27-node hexahedral spectral elements. The typical element size is 1.25 m; the time step was set to Δt = 0.0006 s, and the PML parameters are chosen to be α_0 = 5 and β_0 = 866 s^{-1} [24]. Using the prototype model, we conduct four numerical experiments aimed at assessing primarily the effect of the TRM density on the focusing. Specifically, in the first three experiments we vary the density of the TR mirror (but not its aperture), while in the fourth experiment we randomize the formation's properties.

To generate the recordings at the TRM, we perform a forward wave propagation simulation, initiated by the triggering of two sources, each placed within the two inclusions. The time signal is a Ricker-like pulse with a central frequency of 25 Hz. The inclusion-embedded sources were applied only along the two transverse directions (horizontal) to promote shear waves, since, as discussed in [9], shear waves are more effective in delivering energy at depth than compressional waves; the source amplitudes were set to a nominal 1 N/m^3. Fig. 2(b) and (c) depict displacement wavefield snapshots at two different moments in time during the recording TR step, generated by the simultaneous triggering of two Ricker sources embedded at the center of the inclusions.

4.1. Mirror density effect (Experiments 1 to 3)

4.1.1. Experiment 1 — Full density TR mirror

In Experiment 1, we use the full TRM on $\Gamma_{\mathrm{ID}}^{\mathrm{load}}$, which numbers 16,129 sensors, corresponding roughly to one sensor per mesh node. The recorded displacement histories are time-reversed and applied as tractions, as necessitated by the switching mirror. The maximum amplitude of the applied tractions has been set to a nominal 1 kPa. We note that modern-day actuators mounted on Vibroseis can reach tractions as high as 400 kPa. Thus, the reported displacement fields should be up-scaled by a factor of 300 to 400 to account for field equipment capabilities, while the reported energy metrics should be up-scaled by a factor of 90,000 to 160,000.

Fig. 3(a) shows the average kinetic energy $\mathrm{KE}^{\mathrm{TA}}(\boldsymbol{x})$ during the transmitted step: it can be seen that the waves have refocused at the targets, and the targets have been clearly illuminated.

The illumination is stronger for the left target that is located closer to the ground surface than the right target. This is as expected, due to radiation damping, which forces greater attenuation for the waves reaching the deeper target. Naturally, it would be desirable for both targets to be equally strongly illuminated (or, possibly, be differentially illuminated based on a preset application-driven criterion). A way to achieve wavefields of similar strength at the targets, is by modulating the TRM records prior to time reversal with the desired strength. The graphs of the instantaneous kinetic energies sweeping through the targets are depicted in Fig. 3(b–c): the key difference between the two plots is in the average intensity: the deeper target's intensity is about 35% that of the shallow target's.

Fig. 4 compares the horizontal components of the displacement time histories recorded under the source in the target, between the recording and the transmitting TR steps. For example, the top left plot depicts (solid line) the x-component of the displacement time history at the target during the recording step: it is essentially the "displacement-under-the-load". The same plot also shows (dashed line) the x-component of the displacement time history during the time reversal transmitting step, recorded also at the target. The similarity of the traces, modulo the time delay and the amplitude (the latter has been tuned at the TRM), is evidence of the quality of the refocusing. It can be seen that the shallower target's refocusing is of better quality than that of the deeper target's. We also remark that since at the TRM the tractions were applied along the transverse (horizontal) directions,

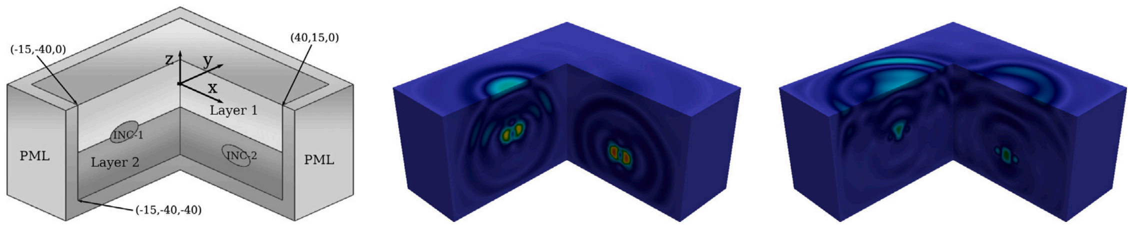

(a) Model schematic (b) Displacement wavefield at t=0.021s (c) Displacement wavefield at t=0.024s

Fig. 2. Schematic of numerical simulations prototype problem; displacement wavefield snapshots during the recording step.

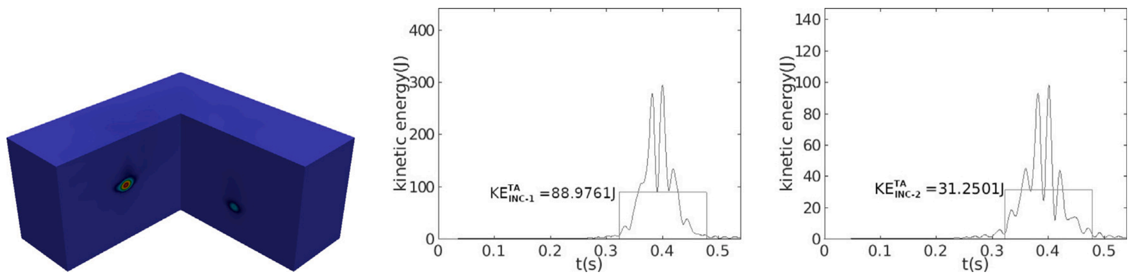

(a) Time-averaged kinetic energy $KE^{TA}(\boldsymbol{x})$ (b) Kinetic energy in the shallow target (c) Kinetic energy in the deep target

Fig. 3. Experiment 1 with full-density TR mirror.

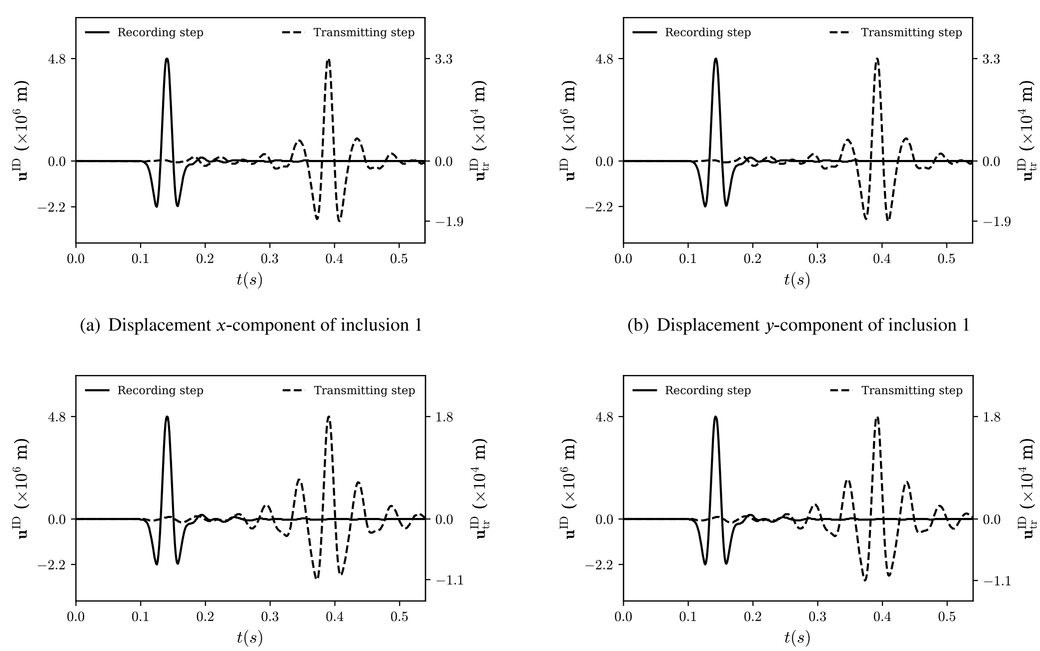

(a) Displacement x-component of inclusion 1 (b) Displacement y-component of inclusion 1

(c) Displacement x-component of inclusion 2 (d) Displacement y-component of inclusion 2

Fig. 4. Displacement time histories at the target; shallow target (left column); deep target (right column); recording step time histories shown with solid line; transmitting step time histories shown with dashed line — Experiment 1.

the z-component records (not shown) are at least an order of magnitude smaller than the horizontal components.

As limited as it may be, due to the unrealistically large number of sensors/emitters, Experiment 1 suggests that focusing to multiple targets is possible using TR, despite the presence of several hostile conditions (domain unboundedness, switching mirror, etc.).

4.1.2. Experiment 2 — Quarter density TR mirror

In the previous experiment, we applied surface tractions on every computational node on the ground surface $\Gamma^{\mathrm{load}}_{\mathrm{ID}}$. Physically, such sensor/actuator deployment is infeasible, and thus, for Experiment 2, we repeat the TR step using a quarter of the TRM, or about 3696 computational nodes where the time-reversed tractions are applied. The number of actuators is still large, and remains practically unrealizable, but the experiment will allow us to further assess the dependence of the focusing on the mirror's density. We note that the aperture remains the same, i.e, the mirror is sparsified, but its spatial extent is unaltered.

Fig. 5(a) depicts again the time-averaged kinetic energy: the targets have been anew illuminated, albeit the magnitude is different owing to the reduced wave energy supplied at the TRM.

The instantaneous kinetic energy $\mathrm{KE}_{\mathrm{INC}}(t)$ is also shown in Fig. 5(b) and (c). The time traces of the displacement wavefield in the inclusions

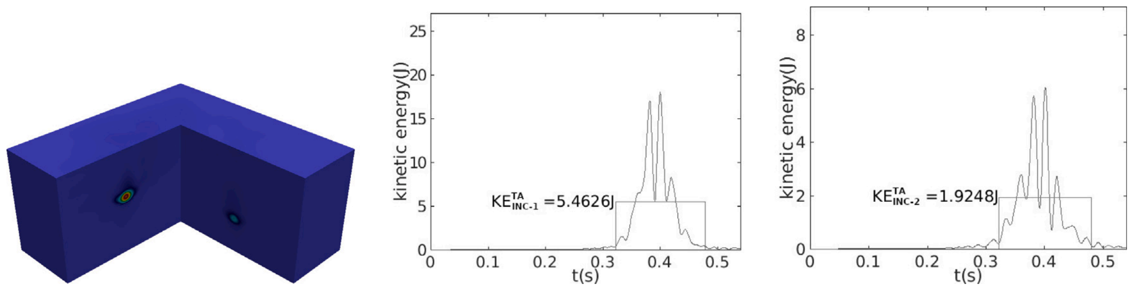

(a) Time-averaged kinetic energy $\mathrm{KE}^{\mathrm{TA}}(\boldsymbol{x})$ (b) Kinetic energy in the shallow target (c) Kinetic energy in the deep target

Fig. 5. Experiment 2 with quarter-density TR mirror.

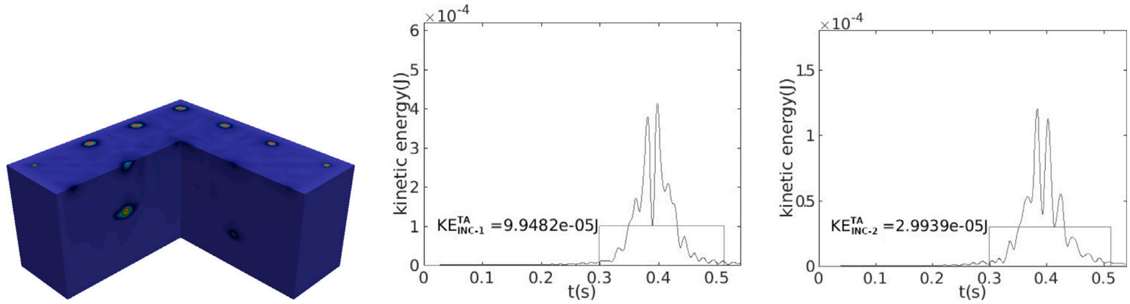

(a) Time-averaged kinetic energy $\mathrm{KE}^{\mathrm{TA}}(\boldsymbol{x})$ (b) Kinetic energy in the shallow target (c) Kinetic energy in the deep target

Fig. 6. Experiment 3 — ultra low TR mirror density.

show similar trends as the ones shown in Fig. 4 for Experiment 1, and are, thus, omitted.

By comparing the Experiment 2 results depicted in Fig. 5 with the corresponding Experiment 1 results depicted in Fig. 3, it can be seen that, qualitatively, the quarter-density TR mirror results are very similar to the full-density mirror results. There are, of course, quantitative differences: the $\mathrm{KE}^{\mathrm{TA}}_{\mathrm{INC}}$ for the shallow target has been reduced from 88.9791 J to 5.4626 J, and for the deep target it has dropped from 31.2501 J to 1.9248 J. For both experiments, the energy efficiency for the shallow target is about 7.7%, and about 2.7% for the deep target. Moreover, the delivered energy to each target in Experiment 2 is about 6% of the corresponding Experiment 1 energy: this percentage is approximately equal to the square of the ratio of the actuators used between the two experiments, i.e., approximately equal to $\left(\frac{3696}{16{,}129}\right)^2$ regardless of the distance between the TRM and the targets. The square of the actuator ratio is a measure of relative energy input. The result is in good agreement with the reports in Anderson et al. [28] and in Koo et al. [9].

4.1.3. Experiment 3 — Ultra low density TR mirror

In Experiment 3 we reduce the TRM density to only 16 actuators –a number that is practically feasible, and repeat the TR simulation. Fig. 6(a) depicts the time-averaged kinetic energy that has helped us before gauge the illumination. Though the targets have been again illuminated as previously in Experiments 1 and 2, the surface TRM actuators are also visible. This is due to the fact that, since the number of actuators is small, the delivered energy to each target is now comparable to the input energy at each actuator. Nevertheless, focusing is still realized. The instantaneous kinetic energy is shown in Fig. 6(b) and (c).

Here, we can confirm that there is no qualitative degradation of $\mathrm{KE}_{\mathrm{INC}}(t)$ when compared with Experiment 1 and 2. However, the values of Experiment 3 are much smaller than those of Experiments 1 and 2 because of the smaller number of TRM actuators. The results of all three experiments are tabulated in Table 1. It can again be verified that the square of the actuator ratios are consistent with the ratios of the delivered energy to the targets.

Table 1
Summary of E_{input}, $\mathrm{KE}^{\mathrm{TA}}_{\mathrm{INC}}$, and delivery efficiency of experiments 1, 2 and 3.

Experiment	E_{input} (J)	Inclusion	$\mathrm{KE}^{\mathrm{TA}}_{\mathrm{INC}}$ (J)	$\mathrm{KE}^{\mathrm{TA}}_{\mathrm{INC}}/E_{input}$
1	1154.15	1	88.98	7.71×10^{-2}
		2	31.25	2.71×10^{-2}
2	71.38	1	5.46	7.77×10^{-2}
		2	1.92	2.70×10^{-2}
3	1.32×10^{-3}	1	9.95×10^{-5}	7.53×10^{-2}
		2	2.99×10^{-5}	2.27×10^{-2}

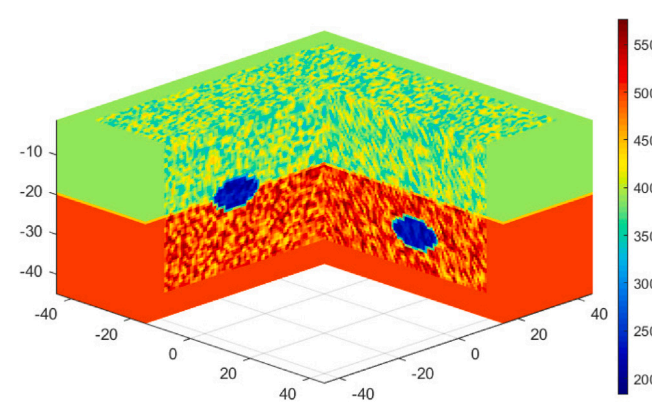

Fig. 7. Shear wave velocity (in m/s) of randomized heterogeneous model.

4.2. Experiment 4 — wave-focusing in a medium of random heterogeneity

In this experiment, we endow the prototype model with random heterogeneity by varying the layer and inclusion properties randomly up to 33% off of their constant values. The resulting property distribution is shown in Fig. 7 for the shear wave velocity. The purpose of the experiment is to explore the effect of the increased scattering induced by the heterogeneity, which is typically beneficial to the focusing.

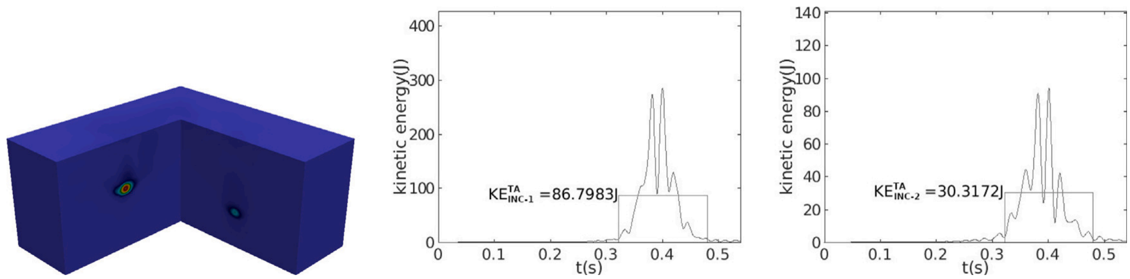

(a) Time-averaged kinetic energy $\mathrm{KE}^{\mathrm{TA}}(\boldsymbol{x})$ (b) Kinetic energy in the shallow target (c) Kinetic energy in the deep target

Fig. 8. Experiment 4 - a randomized heterogeneous medium - full TR mirror density.

The full-density TR mirror is used anew, and the resulting time-averaged distribution $\mathrm{KE}^{\mathrm{TA}}(\boldsymbol{x})$ is shown in Fig. 8(a). When we compare the results in Fig. 8 to those from Experiment 1 (Fig. 3), there are no noticeable qualitative differences; quantitatively, the Experiment 1 energy delivered to the shallow target is 88.9761 J, whereas for Experiment 4, it is about 86.7983 J, a difference of less than 2.5%. Thus, the time reversal approach for wave-focusing appears promising even under arbitrary heterogeneity conditions.

5. Conclusions

Motivated by field applications, in this article, we discussed the problem of focusing energy to multiple subsurface targets embedded within a, generally, heterogeneous semi-infinite host, using an approach based on time reversal. The overarching goal was to improve upon blind surface source excitations that are not informed by the geomorphology and, in general, would not result in focusing energy to the targets. Field constraints necessitate the departure from the ideal implementation of a time-reversal-based approach, which would have guaranteed to focus and result in focusing degradation. As discussed, while the unboundedness of the host, the limited TRM density and aperture, and other reasons play a role in the degradation, the chief cause for the resolution degradation remains the switching TR mirror. However, despite the difficulties, we demonstrated, via numerical simulations, that focusing energy to multiple subsurface targets is feasible. As it can be deduced from Table 1 the energy delivery efficiency depends on the formation's characteristics and would remain the same irrespective of the number of actuators used (the TRM density). For field applications, the computational simulation approach described herein would allow for reasonable estimates of the required surface input energy when given specific energy delivery targets for the inclusions. As the last experiment showed, uncertainties in the subsurface properties would not significantly impact the input energy estimates.

It is noteworthy that the numerical results reported herein complement well recently reported field experiments [29,30].

CRediT authorship contribution statement

Seungbum Koo: Methodology, Software, Validation, Formal analysis, Investigation, Writing – original draft, Visualization. **Heedong Goh:** Conceptualization, Methodology, Writing – review & editing. **Loukas F. Kallivokas:** Conceptualization, Methodology, Writing – original draft, Writing – review & editing, Supervision, Project administration, Funding acquisition.

Declaration of competing interest

The authors declare that they have no known competing financial interests or personal relationships that could have appeared to influence the work reported in this paper.

Data availability

Data will be made available on request.

Acknowledgments

The authors' work was partially supported by an Academic Alliance Excellence grant between the King Abdullah University of Science and Technology in Saudi Arabia (KAUST) and the University of Texas at Austin, United States. The support is gratefully acknowledged.

References

[1] Fink M, Cassereau D, Derode A, Prada C, Roux P, Tanter M, Thomas J-L, Wu F. Time-reversed acoustics. Rep Progr Phys 2000;63(12):1933–95.
[2] Beresnev I, Gaul W, Vigil R. Direct pore-level observation of permeability increase in two-phase flow by shaking. Geophys Res Lett 2011;38(20).
[3] Beresnev I, Johnson P. Elastic-wave stimulation of oil production: A review of methods results. Geophysics 1994;59(6):1000–17.
[4] Roberts P, Esipov I, Majer E. Elastic wave stimulation of oil reservoirs: Promising EOR technology? Lead Edge 2003;22(5):448–53.
[5] Pride S, Flekkøy E, Aursjø O. Seismic stimulation for enhanced oil recovery. Geophysics 2008;73(5):O23–35.
[6] Karve P, Kallivokas LF. Wave energy focusing to subsurface poroelastic formations to promote oil mobilization. Geophys J Int 2015;202(1):119–41.
[7] Jeong C, Kallivokas LF, Kucukcoban S, Deng W, Fathi A. Maximization of wave motion within a hydrocarbon reservoir for wave-based enhanced oil recovery. J Pet Sci Eng 2015;129:205–20.
[8] Karve P, Fathi A, Poursartip B, Kallivokas LF. Source parameter inversion for wave energy focusing to a target inclusion embedded in a three-dimensional heterogeneous halfspace. Int J Numer Anal Methods Geomech 2017;41:1016–37.
[9] Koo S, Karve P, Kallivokas LF. A comparison of time-reversal and inverse-source methods for the optimal delivery of wave energy to subsurface targets. Wave Motion 2016;67:121–40.
[10] Jeong C, Kallivokas LF. An inverse-source problem for maximization of pore-fluid oscillation within poroelastic formations. Inverse Prob Sci Eng 2017;25(6):832–63.
[11] Ing RK, Fink M. Time recompression of dispersive lamb waves using a time reversal mirror-application to flaw detection in thin plates. In: 1996 IEEE ultrasonics symposium. Proceedings, Vol. 1. 1996, p. 659–63, vol.1.
[12] Park HW, Sohn H, Law KH, Farrar CR. Time reversal active sensing for health monitoring of a composite plate. J Sound Vib 2007;302(1):50–66.
[13] Shustak M, Landa E. Time reversal based detection of subsurface scatterers. In: SEG technical program expanded abstracts 2017. 2017, p. 969–73.
[14] Anderson BE, Ulrich TJ, Le Bas P-Y, Ten Cate JA. Three-dimensional time reversal communications in elastic media. J Acoust Soc Am 2016;139(2):EL25–30.
[15] Norville PD, Scott Jr WR. Time-reversal focusing of elastic surface waves. J Acoust Soc Am 2005;118(2):735–44.
[16] Larmat C, Montagner J-P, Fink M, Capdeville Y, Tourin A, Clévédé E. Time-reversal imaging of seismic sources and application to the great Sumatra earthquake. Geophys Res Lett 2006;33(19).
[17] Larmat CS, Guyer RA, Johnson PA. Time-reversal methods in geophysics. Phys Today 2010;63(8):31–5.
[18] Steiner B, Saenger E, Schmalholz S. Time reverse modeling of low-frequency microtremors: Application to hydrocarbon reservoir localization: Direct pore-level observation of permeability increase in two-phase flow by shaking. Geophys Res Lett 2008;35(3).
[19] Larmat C, Guyer R, Johnson P. Tremor source location using time reversal: Selecting the appropriate imaging field. Geophys Res Lett 2009;36(22).
[20] Artman B, Podladtchikov I, Witten B. Source location using time-reverse imaging. Geophysical prospecting. Geophys Res Lett 2010;58(5):861–73.

[21] Nakata N, Beroza G. Reverse time migration for microseismic sources using the geometric mean as an imaging condition. Geophysics 2016;81(2):KS51–60.

[22] Yang J, Zhu H. Locating and monitoring microseismicity, hydraulic fracture and earthquake rupture using elastic time-reversal imaging. Geophys J Int 2019;216(1):726–44.

[23] Karve PM, Kucukcoban S, Kallivokas LF. On an inverse source problem for enhanced oil recovery by wave motion maximization in reservoirs. Comput Geosci 2015;19(1):233–56.

[24] Fathi A, Poursartip B, Kallivokas LF. Time-domain hybrid formulations for wave simulations in three-dimensional PML-truncated heterogeneous media. Internat J Numer Methods Engrg 2015;101(3):165–98.

[25] Cassereau D, Fink M. Focusing with plane time-reversal mirrors: An efficient alternative to closed cavities. J Acoust Soc Am 1993;94(4):2373–86.

[26] Goh H, Koo S, Kallivokas LF. Resolution improving filter for time-reversal (TR) with a switching TR mirror in a halfspace. J Acoust Soc Am 2019;145(4):2328–36.

[27] Koo S. Subsurface elastic wave energy focusing based on a time reversal concept (Ph.D. thesis), The University of Texas at Austin; 2017, URL: http://hdl.handle.net/2152/61529.

[28] Anderson BE, Guyer RA, Ulrich TJ, Johnson PA. Time reversal of continuous-wave, steady-state signals in elastic media. Appl Phys Lett 2009;94(11):111908.

[29] Landa E, Yurman A, Jenneskens R. Seismic time reversal mirror experiment. First Break 2019;37(6):41–5.

[30] Keydar S, Landa E. Wave refocusing for linear diffractor using the time-reversal principle. Geophys Prospect 2019;67(5):1345–53.